ACS OMEGA

http://pubs.acs.org/journal/acsodf

Article

The Strain-Tuned Spin Seebeck Effect, Spin Polarization, and Giant Magnetoresistance of a Graphene Nanobubble in Zigzag Graphene Nanoribbons

Yun Ni,* Gang Deng, Jia Li, Hu Hua, and Na Liu

Cite This: *ACS Omega* 2021, 6, 15308−15315

Read Online

ACCESS | Metrics & More | Article Recommendations

ABSTRACT: By using first-principle calculations combined with the non-equilibrium Green's function approach, we studied the spin caloritronic properties of zigzag graphene nanoribbons with a nanobubble at the edge (NB-ZGNRs). The thermal spin-polarized currents can be induced by a temperature difference, and the spin Seebeck effect is found in the nanoribbon. The spin polarization, magnetoresistance, and Seebeck coefficients are discussed, which are strongly affected and can be tuned by the geometrical strain. Moreover, some novel spin caloritronic devices are designed, such as a device that generates bidirectional perfect spin currents and thermally induced giant magnetoresistances. Our results open up the possibility of tuning the spin caloritronic properties of the NB-ZGNR-based devices by changing the elastic strain on the graphene nanobubble.

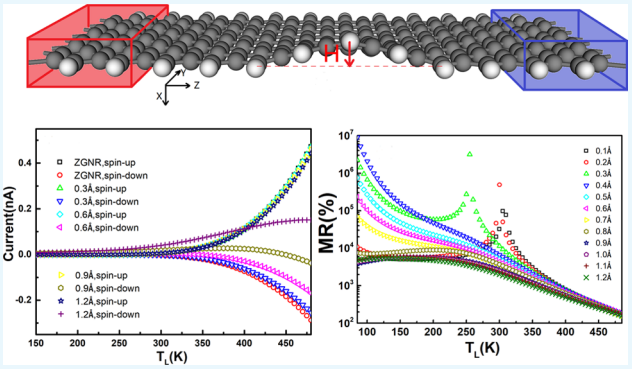

1. INTRODUCTION

As the world's energy demand continues to grow, traditional energy sources will gradually dry up, and it is particularly important to develop new materials to provide sustainable green energy for the future. One promising resolution lies on thermoelectric materials, which reveal the interplay of heat and charge transport.[1−4] Meanwhile, spintronics, which concerns the interplay of spin and charge transport, has been recognized as a promising technology to complement conventional silicon-based electronics.[5−8] Recently, spin caloritronics, which combines thermoelectrics and spintronics, mainly focusing on heat and spin transport, has attracted great attention.[9−11] A notable recent finding of spin caloritronics is the observation of the spin Seebeck effect by Uchida et al.,[12,13] where the spin current and associated spin voltage are produced by a temperature gradient and the spin-polarized currents flow in opposite directions. To obtain a remarkable spin Seebeck effect, many researchers have focused their research on low-dimensional nanomaterials, particularly one-dimensional nanoribbons and nanowires.[14−17]

Meanwhile, graphene nanoribbons (GNR), which exhibit various spintronic and thermoelectric properties, have attracted much attention and are one of the most promising candidate materials for future electronic devices.[9,16,18,19] In particular, zigzag-edged graphene nanoribbons (ZGNRs) are more notable because of its spin-resolved electronic and transport properties.[20−23] At present, a lot of spintronic and spin caloritronic devices based on ZGNRs are realized in theoretical and experimental studies,[24,25] and even the spin Seebeck effect also has been found in ZGNRs.[9,18,26] However, it is worth noting that graphene is able to form nanosize bubbles by trapping gas molecules under high pressure[27,28] or growing in ultrahigh vacuum.[29] Theoretically, the presence of the graphene nanobubble may cause elastic strain and modification on electron density, affecting the electron-hopping amplitude between carbon atoms.[30] For instance, researchers have found that the graphene nanobubbles can induce pseudomagnetic fields greater than a value of 300 T at room temperature.[29] Whether the spin Seebeck effect of the ZGNR is affected by the geometrical strains caused by the graphene nanobubble or not is a matter of great concern.

As we know, the graphene nanobubbles always appear in two-dimensional graphene sheets during the experimental preparation.[29,31,32] The graphene nanobubble may be split in half when the edge of the ZGNR is located on the nanobubble during the cutting process. In this paper, we consider the structure that a half nanobubble locates at the edge since the

Received: March 26, 2021
Accepted: May 25, 2021
Published: June 2, 2021

electron transport properties are mostly depended on the edge states of the ZGNR. The results show that the spin Seebeck effect of the NB-ZGNR is greatly influenced by the local geometrical strain at the edge. Moreover, the elastic strain induced by the nanobubble can tune the spin caloritronic properties of the NB-ZGNR.

2. RESULTS AND DISCUSSION

As shown in Figure 1, the 8-ZGNR nanoribbon with 8 zigzag carbon chains is selected to construct the devices,[33] and the

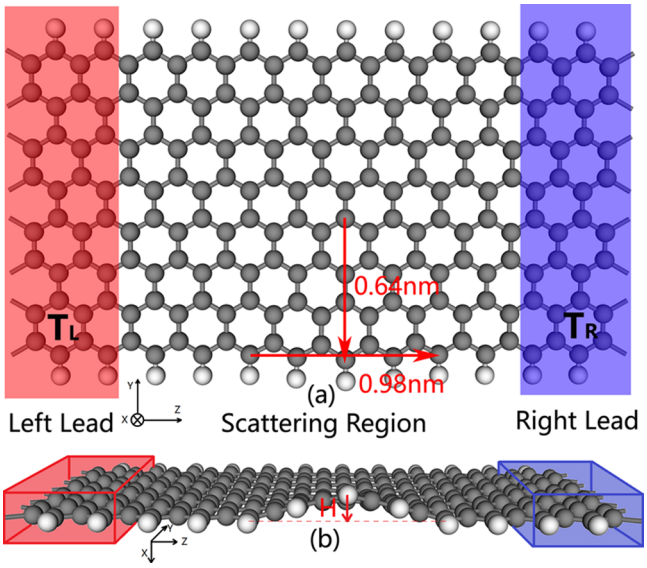

Figure 1. Schematic device model of the two-probe system of the defected ZGNR with the graphene nanobubble. (a) Top view and (b) side view. The red frame indicates the semi-infinite left leads, while the blue one indicates the semi-infinite right leads. The transmission direction is along the z direction.

scale of the half nanobubble is marked in the figure. The height of the nanobubble is adjustable and is set to H (from 0.1 to 1.2 Å) in our study to achieve varying degrees of geometrical strains. Notice that the left and right electrodes are semi-infinite, the scattering region includes the nanobubble and the buffer layers, and all the dangling bonds at the edges are passivated with hydrogen atoms.

Since the spin orientation of the ZGNR electrodes can be tuned by an external magnetic field, the magnetic field is applied on the electrodes, and the electrodes are all ferromagnetic. The magnetization configuration of the device can be set to parallel configuration (PC): the magnetic fields of left and right electrodes are set in the same direction (both up) or antiparallel configuration (APC): the magnetic fields of left and right electrodes are set in the opposite directions (left is up and right is down). We have calculated the thermally induced spin-dependent currents of the NB-ZGNR devices in both PC and APC magnetization configurations, and the results are shown in Figure 2. The heights of the nanobubble (H) are chosen at 0.3, 0.6, 0.9, and 1.2 Å. Meanwhile, the results of the ideal ZGNR-based device in PC and APC are also shown in the figure to make a comparison.

In PC, obvious spin Seebeck effects can be seen in ZGNRs and parts of NB-ZGNRs, whose spin-up currents are positive while the spin-down ones are negative. The spin-resolved current curves versus T_L (ΔT = 20 K) and ΔT (T_L = 380 K) are plotted in Figure 2a,b. As the height of the nanobubble increases, the positive spin-up current curves remain nearly constant, which means that the enhanced geometrical strain has no effect on the spin-up currents in NB-ZGNRs. However, with the nanobubble's height increasing, the negative spin-down current curves decrease rapidly, eventually reverse, and then increase in the opposite direction, which is greatly affected by the geometrical strain. In some NB-ZGNRs, the spin Seebeck effects are gradually weaken or even disappeared. For instance, when the height of the nanobubble reaches 1.2 Å, the spin Seebeck effect is completely unobservable, and we can only obtain the thermal spin-up and spin-down currents in just one direction (positive).

In APC, the thermally induced spin-polarized currents are also obtained in the device, but the spin-up and spin-down currents are both negative and no obvious spin Seebeck effects can be seen. As seen from the spin-resolved current curves versus T_L (ΔT = 20 K) and ΔT (T_L = 380 K) in Figure 2c,d, the values of spin-down currents are much larger than the spin-up ones, and both of them are getting larger with the increasing height of the nanobubble. When the heights of the nanobubble reach 0.9 and 1.2 Å, the values of thermal spin-down currents are nearly proportional to T_L (Figure 2c), with curve slopes of -2.10×10^{-12} and -2.97×10^{-12}, respectively.

Since the spin polarization is one of the most important parameters of the spin caloritronic device, we have calculated the spin polarizations (SPs) of all the devices using SP (%) = ($|I_{up}| - |I_{down}|$)/($|I_{up}| + |I_{down}|$) × 100, and the results are shown in Figure 3. The vertical coordinates represent the height of the nanobubble (H), where H = 0.0 means the ZGNR-based device. Because of the aggravating heat dissipation of electronic devices in practical applications, we mainly focus on the SPs at room and elevated temperatures. As we can see from Figure 3a, in PC, the ZGNR-based device has a large SP at low temperatures (T_L < 250 K), and the SP decreases rapidly with the temperature increasing. At room temperature, the SP of ZGNRs is as low as 12.7%. However, due to the influence of geometrical strain, the SPs of NB-ZGNRs have changed a lot, which increase at room and elevated temperatures. With the nanobubble's height increasing, from the device H = 0.4 Å, the SPs of NB-ZGNRs can reach nearly 100% (complete polarization) in a certain temperature range (the red zone) at room and elevated temperatures. The corresponding temperatures for complete spin polarization rise as the height of the nanobubble increases, and the applicable temperature range gets larger. By changing the strain of the device, we can tune and control the spin polarization of the nanoribbon and obtain the completely spin-polarized current in a certain temperature range at room and elevated temperatures. As seen from Figure 3b, when the T_L is fixed at 380 K, the variation of SP versus ΔT is relatively small, which means that spin polarization is less affected by the temperature difference. In this case from the figure, the completely spin-polarized currents are mainly obtained in the devices H = 0.6 and 0.7 Å, but since establishing a huge temperature difference in such a small device is rather difficult in practice, a NB-ZGNR-based device with H = 0.7 Å is the optimum device configuration to obtain a perfect spin polarization effect at 380 K. Therefore, in practical applications, we can tune the elastic strain of the nanobubble according to the working temperature of the device to generate a completely spin-polarized thermal current.

Meanwhile, in APC, the spin polarizations are much higher than those of PC, and all of them are almost greater than 70%.

https://doi.org/10.1021/acsomega.1c01640
ACS Omega 2021, 6, 15308−15315

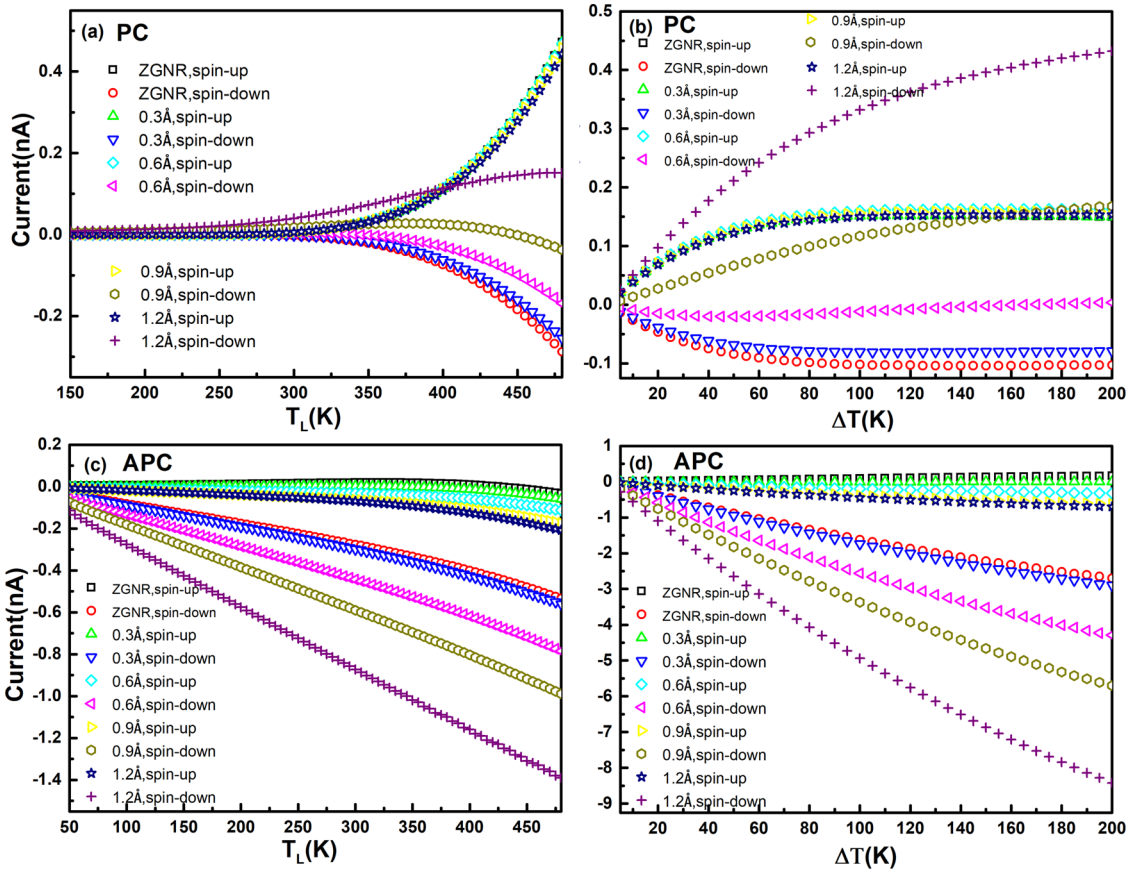

Figure 2. Thermal spin-dependent current curves versus T_L (a, c) and ΔT (b, d) in PC and APC magnetization configurations.

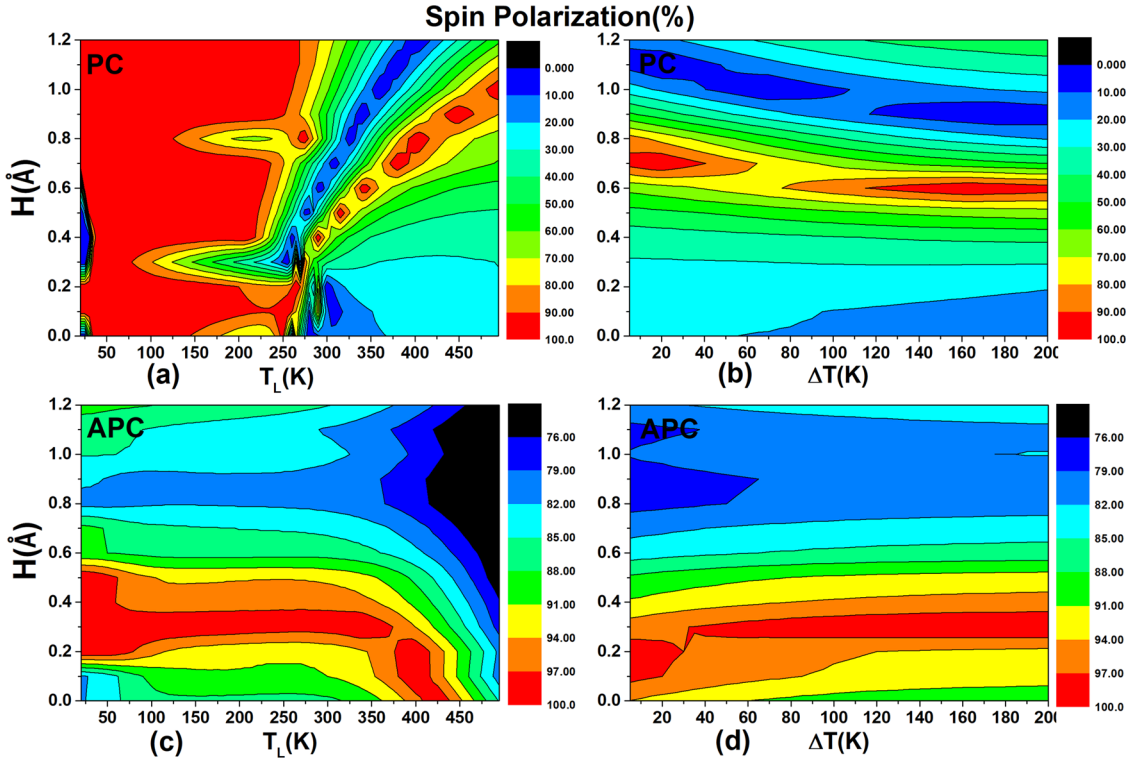

Figure 3. Contour graphs of spin polarization (%) in PC and APC. (a, c) Versus H and T_L; (b, d) versus H and ΔT.

As seen from Figure 3c,d, the spin polarization in the red zone is extremely close to 100%, which is almost a perfect spin polarization. Both the T_L and ΔT have less effect on the spin polarization, and in contrast, the elastic strain plays a key role

https://doi.org/10.1021/acsomega.1c01640
ACS Omega 2021, 6, 15308−15315

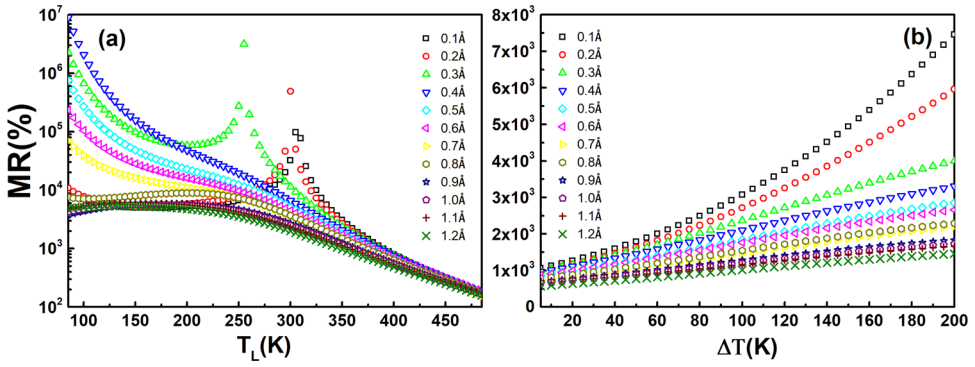

Figure 4. Magnetoresistance (MR) as a function of T_L (a) and ΔT (b) of the devices with different H.

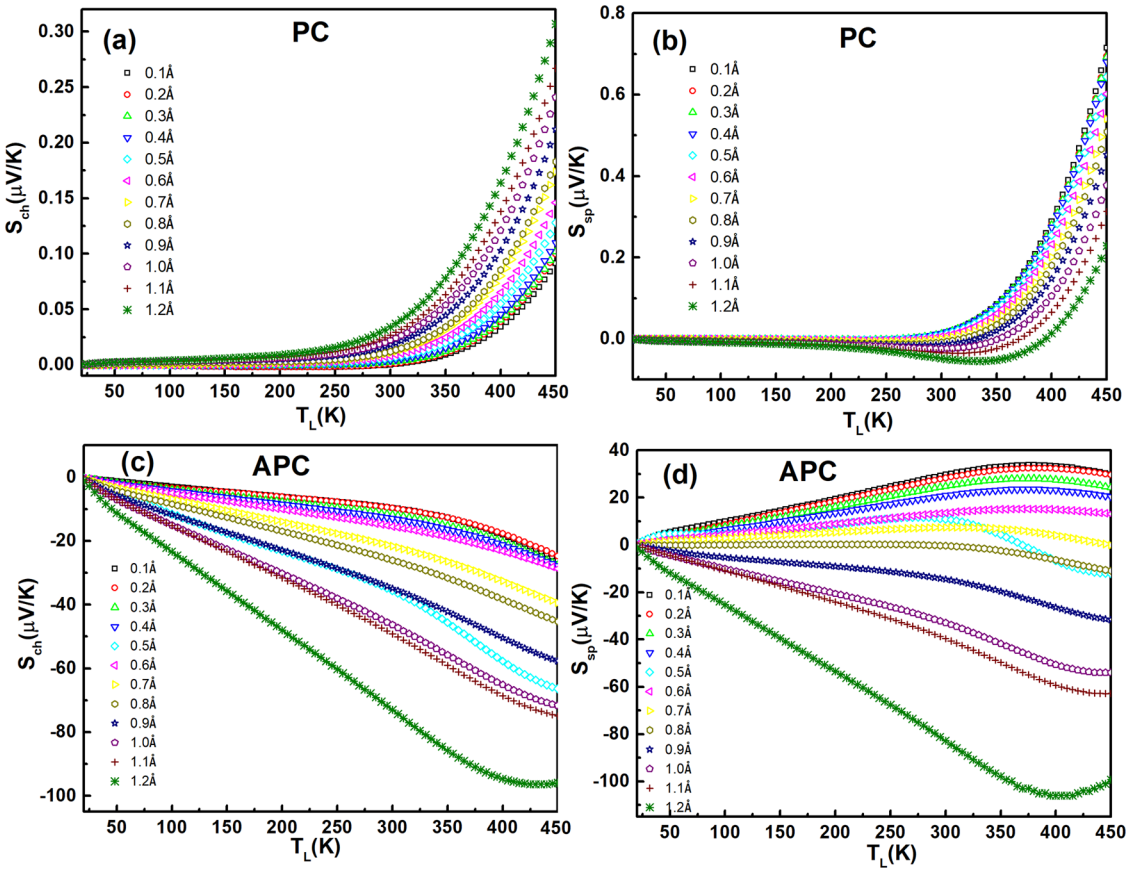

Figure 5. (a, c) Charge Seebeck coefficient (S_{ch}) and (b, d) spin Seebeck coefficient (S_{sp}) as a function of T_L in PC and APC.

in spin polarization. In this case, the NB-ZGNR device with H = 0.3 Å can achieve perfect spin polarization over an extremely wide temperature range, which can be used to generate a perfect spin-polarized thermal current in application. Since the total current directions of PC and APC are opposite (Figure 2), and both can achieve perfect spin polarization through geometrical strain, we can use it to obtain a NB-ZGNR-based device to generate a perfect bidirectional spin-polarized current, which means that we can obtain either a forward or reverse spin current with nearly 100% spin polarization by setting the appropriate magnetic orientations and temperature differences.

Since the spin orientation of the electrode can be controlled by the magnetic field direction, we can alter the device magnetic configuration from APC to PC by changing the directions of the magnetic fields. The corresponding magnetoresistance (MR) can be obtained from the equation MR (%) = $(R_{PC} - R_{APC})/(R_{APC}) \times 100 = [(I_{APC} - I_{PC})/I_{PC}] \times 100$, where I_{APC} and I_{PC} are the total currents in the APC and PC, respectively. As seen from Figure 4a, when the temperature is very low (T_L < 200 K), all the NB-ZGNR-based devices have a large value of thermal MRs, greater than 10^3%. Thereinto, the MRs of five devices, whose nanobubble heights are 0.3, 0.4, 0.5, 0.6, and 0.7 Å, are greater than 10^4%; when the heights are 0.3 and 0.4 Å, MRs can even be greater than 10^6% at extremely low temperatures. However, since the applicable temperatures are too low, these giant MRs cannot be used practicably in the industry application. As the temperature (T_L) increases, the MR values of most devices gradually decrease and eventually fall below 10^3% at about 400 K. However, the MR curves of three devices with nanobubble heights of 0.1, 0.2, and 0.3 Å are somewhat different: a peak around room temperature

https://doi.org/10.1021/acsomega.1c01640
ACS Omega 2021, 6, 15308−15315

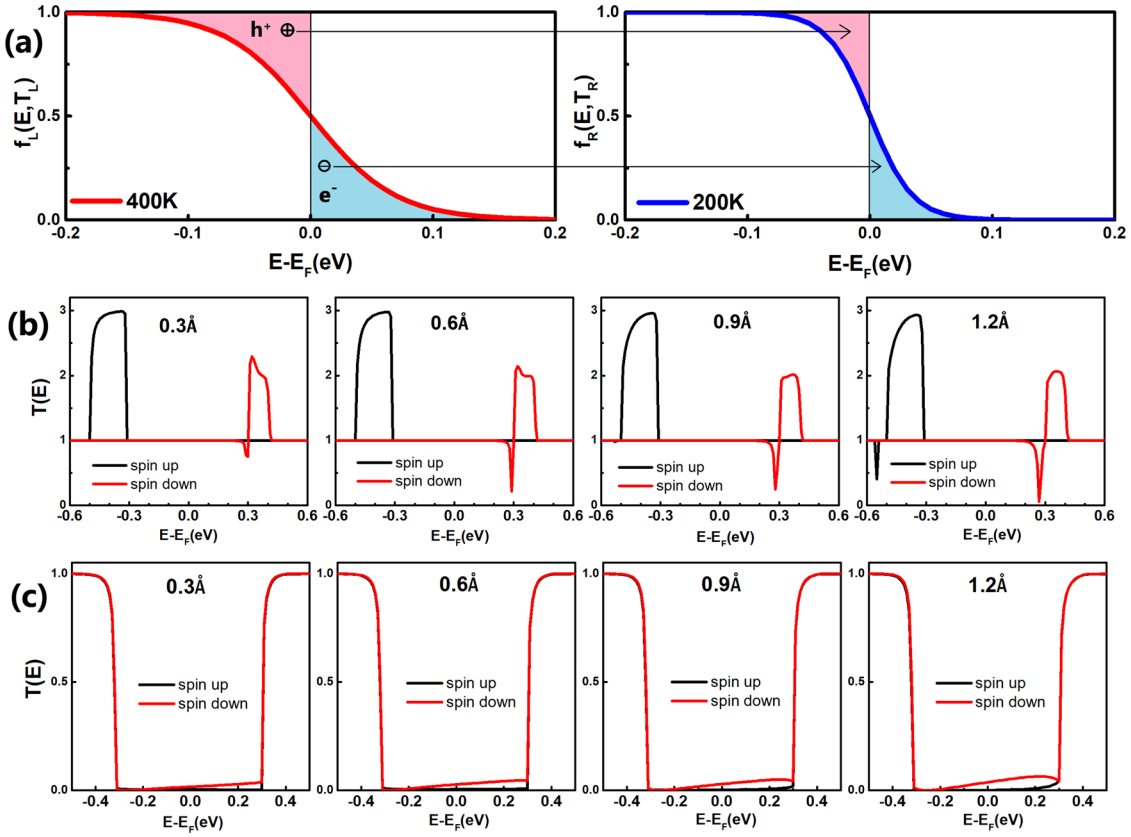

Figure 6. (a) Fermi distribution of the left electrode (the left panel, higher temperature) and the right electrode (the right panel, lower temperature). The spin-dependent transmission spectra in (b) PC and (c) APC are shown, and the H values are set to 0.3, 0.6, 0.9, and 1.2 Å.

appearing on the MR curve. The peak value of the device H = 0.3 Å appears around 255 K, while the peak values of devices H = 0.1 and 0.2 Å appear around 305 and 300 K, respectively. Thus, when the temperature is greater than 200 K, the MR of the device H = 0.3 Å can remain greater than 10^5% within a temperature range [240 and 260 K] and greater than 10^4% until 300 K; the MR of the device H = 0.1 Å can remain greater than 10^4% within a temperature range [280 and 320 K]; the MR of the device H = 0.2 Å can remain greater than 10^4% within a temperature range [270 and 315 K]. As seen from Figure 4b, the temperature difference also has an effect on the value of MR, which grows a lot with ΔT increasing, but the magnitude change is smaller than T_L. Moreover, as seen from the growth of the curves, the device with less geometrical strain is more affected by the temperature difference. Making use of these properties, we can use NB-ZGNR to construct thermal giant MR (GMR) device, whose value can be tuned by the structure strain. According to the actual temperature, we can choose the suitable strain and obtain an optimum MR. For instance, around room temperature, the optimum heights of nanobubbles should be 0.1, 0.2, and 0.3 Å, and then high MRs can be obtained.

The charge Seebeck coefficient (S_{ch}) and spin Seebeck coefficient (S_{sp}) of the NB-ZGNR-based devices are calculated, and the corresponding curves versus T_L in PC and APC are plotted in Figure 5. As the height of the nanobubble changes from 0.1 to 1.2 Å, the S_{ch} increases and remains positive, as seen in Figure 5a, which indicates that the device is hole-conducting in PC. Meanwhile, in APC, as seen in Figure 5c, the absolute value of S_{ch} also increases with the geometrical strain increasing but the value remains negative, which indicates that the device is electron-conducting in this configuration. Hence, the NB-ZGNR-based devices can transfer between electron-conducting (APC) and hole-conducting (PC) by adjusting the magnetic field direction of the electrode. The spin Seebeck coefficient is defined as $S_{sp} = S_\uparrow - S_\downarrow$, where $S_\uparrow$ and $S_\downarrow$ are the Seebeck coefficients of spin-up and spin-down channels, respectively, and the S_{sp} curves in PC and APC are shown in Figure 5b and Figure 5d, respectively. In PC, the S_{sp} curve decreases with the height increasing. When the temperature is not high, the S_{sp} decreases first and then increases negatively. When the temperature is higher than 400 K, all the S_{sp} values remain positive and decrease with the increasing strain. In APC, some devices have S_{sp} greater than zero while others are less than zero, which mainly depend on the heights of the nanobubbles. With the strain increasing, the S_{sp} curve decreases and those of H = 0.6 and 0.7 Å are down to nearly zero, so the spin Seebeck effect weakens. As the strain continues to increase by exceeding H = 0.8 Å, the S_{sp} values are all negative and their absolute values increase rapidly. The negative maximum value of S_{sp} is shown in the device H = 1.2 Å near 400 K. We also note that, among all devices in APC, the device H = 0.5 Å shows a great different trend in the S_{ch} and S_{sp} curves versus T_L. In a word, these results tell us that we can use the geometrical strain to tune the spin Seebeck effect of the NB-ZGNR-based device.

At last, we discuss the causes of the thermally induced currents and spin Seebeck effects, which mainly depend on the interaction of electrodes' Fermi−Dirac distributions and asymmetric spin-polarized transmission spectra. To understand the fundamental mechanism of the properties, it is necessary to analyze the electron distributions and the carrier concen-

https://doi.org/10.1021/acsomega.1c01640
ACS Omega 2021, 6, 15308−15315

trations of the left and right electrodes, which are determined by the Fermi–Dirac distribution. The Fermi–Dirac distributions of T_L = 400 K and T_R = 200 K are shown in Figure 6a, which is defined as $f(E, T) = \frac{1}{\exp[(E-\mu)/kT]+1}$, where μ is the chemical potential. There are two conditions for carrier transport: The first is that a carrier (electron) with an energy higher than the Fermi level flows from the left electrode to the right one because the electron distribution of the left electrode is higher than that of the right one, thus generating a negative current I_e. The second is a carrier (hole) with an energy below the Fermi level, which also flows from left to right because the electrons at the left are less distributed than at the right, producing a positive current I_h. If the transmission spectrum is symmetric, then I_e and I_h will cancel each other out and no thermal current can be obtained. However, if the transmission spectrum is asymmetric, then the thermally induced current will be a negative electron current or a positive hole current, which depends on the transport channels above and below the Fermi level. In addition, we mainly focus on the electron transmission with temperature differences, and the effect of the phonon is neglected here.

The spin-polarized transport spectra of NB-ZGNRs with heights of 0.3, 0.6, 0.9, and 1.2 Å are shown in Figure 6b,c, including PC and APC. In PC, the spin-up transport spectra have a high transport peak below the Fermi level, while the spin-down transport spectra have a large transport peak above the Fermi level. Thus, the spin-up thermal currents are positive since the positive hole currents dominate, while the spin-down thermal currents are negative since the negative electron currents dominate, and the spin Seebeck effects appear (Figure 2a). As the height of the nanobubble increases, the spin-up transport spectrum changes a little, and just a tiny valley appears at −0.54 eV in the spectrum of the device H = 1.2 Å, which is quite far away from the Fermi level and has little effect on the carrier transport. That is why the spin-up current curves are almost constant as the geometrical strain changes. At the same time, the spin-down transport spectrum shows an obvious transmission valley not far from and above the Fermi level, which becomes deeper and deeper with the strain increasing, so the absolute value of the spin-down current decreases gradually. When the height of the nanobubble reaches 1.2 Å, the nadir of the transport valley is as low as 0.05, very close to zero, with few transmission channels above the Fermi level. Therefore, the positive hole current plays a dominant role in the device H = 1.2 Å, the thermal spin-down current is positive, and the spin Seebeck effect disappears (Figure 2a).

In APC, since the spin-up spectrum is almost symmetrical to the devices with different H, the thermal spin-up current is quite small all the time. As the strain increases, the spin-up transport spectrum above the Fermi level just increases slightly, so the electron current is dominant and the thermal spin-up current is negative with just a little change. At the same time, due to the obvious asymmetry of the spin-down transport spectrum, the thermal spin-down current is dominated by electron currents, so the spin-down current is negative and quite large. With the increase in strain, the asymmetry of the transport spectrum is enhanced, and the transport channels above the Fermi level is increased, which makes the value of the thermal spin-down current increase rapidly (Figure 2c).

3. CONCLUSIONS

In summary, the spin caloritronic properties of NB-ZGNRs have been investigated using the NEGF-DFT approach. By changing the geometrical strain, the thermally induced transport properties of the devices can be tuned, such as the thermally induced current, the spin Seebeck effect, the spin polarization, and the thermally induced magnetoresistance. The mechanisms and causes of these properties can be explained by the spin-polarized transport spectra and Fermi–Dirac distributions in our study. By applying the appropriate temperature difference and geometrical strain and changing the directions of the electrode magnetic fields, we obtained the NB-ZGNR-based spin caloritronic device that can generate a perfect bidirectional spin-polarized current. We also predicted that, under the temperature gradient, the GMR can be obtained around room temperature in the NB-ZGNR-based device, the value of which is also related to the geometrical strain of the nanoribbon.

4. METHODS

Our first-principles calculations are based on the Nanodcal quantum transport package, which adopts spin density functional theory combined with the nonequilibruim Green's function (NEGF).[34,35] The NEGF transport model in the Nanodcal package is that the boundary conditions are not periodic in the transport C-direction. Since our devices are one-dimensional systems, with vacuum layers of more than 15 Å in these two directions, the k_A and k_B were all set to one. Furthermore, we needed a lot of k_C-points in the electrode calculation to match the Fermi level of the electrodes and the central region. Therefore, the value of k_C = 100 was set to preserve the accuracy of the results. The calculation was carried out using the framework of density functional theory with the spin-polarized generalized gradient approximation and Perdew–Burke–Ernzerhof exchange correlation functional, and core electrons were described by norm-conserving pseudopotentials.[36,37] A single-polarized basis set was used, the cutoff energy was 150 Ry, and the convergence parameters of the optimization were chosen as follows: a total energy tolerance of 1×10^{-5} eV/atom and a maximum force tolerance of 0.01 eV/Å. The NEGF-DFT self-consistency was controlled by a numerical tolerance of 10^{-5} eV. The spin-dependent current through the system was calculated using the Landauer formula:[38]

$$I^{\uparrow(\downarrow)} = \frac{e}{h}\int_{-\infty}^{\infty}\{T^{\uparrow(\downarrow)}(E)[f_L(E,\mu) - f_R(E,\mu)]\}\,dE \quad (1)$$

where $f_{L(R)}(E,\mu)$ is the equilibrium Fermi distribution for the left (right) electrode, $\mu_{L,R} = E_F \pm$ eV/2 is the electrochemical potentials of the left and right electrodes in terms of the common Fermi energy E_F, and $T^{\uparrow(\downarrow)}(E)$ is the spin-resolved transmission defined as

$$T^{\uparrow(\downarrow)}(E) = Tr[\Gamma_L G^R \Gamma_R G^A]^{\uparrow(\downarrow)} \quad (2)$$

where $G^{R(A)}$ is the retarded (advanced) Green's functions of the central region and $\Gamma_{L(R)}$ is the coupling matrix of the left (right) electrode. In spin caloritronic calculations, we mainly focus on the spin-dependent currents driven by the temperature difference between the source and the drain ($\Delta T = T_R - T_L$), without any external bias, and $\mu_L = \mu_R = E_F$ (Fermi level) is set to zero.

https://doi.org/10.1021/acsomega.1c01640
ACS Omega 2021, 6, 15308−15315

AUTHOR INFORMATION

Corresponding Author

Yun Ni − *Hubei Engineering Technology Research Center of Energy Photoelectric Device and System and College of Science, Hubei University of Technology, Wuhan 430068, China;* orcid.org/0000-0003-2085-7936; Email: niyun1109@126.com

Authors

Gang Deng − *Hubei Engineering Technology Research Center of Energy Photoelectric Device and System and College of Science, Hubei University of Technology, Wuhan 430068, China*

Jia Li − *Hubei Engineering Technology Research Center of Energy Photoelectric Device and System and College of Science, Hubei University of Technology, Wuhan 430068, China*

Hu Hua − *Hubei Engineering Technology Research Center of Energy Photoelectric Device and System and College of Science, Hubei University of Technology, Wuhan 430068, China*

Na Liu − *College of Physics and Electronic Science, Hubei Normal University, Huangshi 435002, China*

Complete contact information is available at: https://pubs.acs.org/10.1021/acsomega.1c01640

Notes

The authors declare no competing financial interest.

ACKNOWLEDGMENTS

This work was supported by the National Natural Science Foundation of China under grant no. 11404119, by the Doctoral Scientific Research Foundation of Hubei University of Technology (grant no. BSQD2020106), by the Program for Innovative Teams of Outstanding Young, and the Middle-aged Researchers in the Higher Education Institutions of Hubei Province (grant no. T2020014).

REFERENCES

(1) DiSalvo, F. J. Thermoelectric Cooling and Power Generation. *Science* **1999**, *285*, 703−706.

(2) Sales, B. C. Smaller Is Cooler. *Science* **2002**, *295*, 1248−1249.

(3) Boukai, A. I.; Bunimovich, Y.; Tahir-Kheli, J.; Yu, J.-K.; Goddard Iii, W. A.; Heath, J. R. Silicon Nanowires as Efficient Thermoelectric Materials. *Nature* **2008**, *451*, 168−171.

(4) Ding, G.; Gao, G.; Yao, K. High-Efficient Thermoelectric Materials: The Case of Orthorhombic Iv-Vi Compounds. *Sci. Rep.* **2015**, *5*, 1−7.

(5) Wolf, S.; Awschalom, D.; Buhrman, R.; Daughton, J.; von Molnár, v. S.; Roukes, M.; Chtchelkanova, A. Y.; Treger, D. Spintronics: A Spin-Based Electronics Vision for the Future. *Science* **2001**, *294*, 1488−1495.

(6) Ni, Y.; Wang, X.; Tao, W.; Zhu, S.-C.; Yao, K.-L. The Spin-Dependent Transport Properties of Zigzag A-Graphyne Nanoribbons and New Device Design. *Sci. Rep.* **2016**, *6*, 1−10.

(7) Šmejkal, L.; Mokrousov, Y.; Yan, B.; MacDonald, A. H. Topological Antiferromagnetic Spintronics. *Nat. Phys.* **2018**, *14*, 242−251.

(8) Ding, L.; Zhong, Y. A Theoretical Strategy for Pressure-Driven Ferroelectric Transition Associated with Critical Behavior and Magnetoelectric Coupling in Organic Multiferroics. *Phys. Chem. Chem. Phys.* **2020**, *22*, 19120−19130.

(9) Zeng, M.; Feng, Y.; Liang, G. Graphene-Based Spin Caloritronics. *Nano Lett.* **2011**, *11*, 1369−1373.

(10) Bauer, G. E.; Saitoh, E.; Van Wees, B. J. Spin Caloritronics. *Nat. Mater.* **2012**, *11*, 391−399.

(11) Sierra, J. F.; Neumann, I.; Cuppens, J.; Raes, B.; Costache, M. V.; Valenzuela, S. O. Thermoelectric Spin Voltage in Graphene. *Nat. Nanotechnol.* **2018**, *13*, 107−111.

(12) Uchida, K.; Takahashi, S.; Harii, K.; Ieda, J.; Koshibae, W.; Ando, K.; Maekawa, S.; Saitoh, E. Observation of the Spin Seebeck Effect. *Nature* **2008**, *455*, 778−781.

(13) Uchida, K.-i.; Xiao, J.; Adachi, H.; Ohe, J.-i.; Takahashi, S.; Ieda, J.; Ota, T.; Kajiwara, Y.; Umezawa, H.; Kawai, H.; Bauer, G. E. W.; Maekawa, S.; Saitoh, E. Spin Seebeck Insulator. *Nat. Mater.* **2010**, *9*, 894−897.

(14) Golberg, D.; Bando, Y.; Huang, Y.; Terao, T.; Mitome, M.; Tang, C.; Zhi, C. Boron Nitride Nanotubes and Nanosheets. *ACS Nano* **2010**, *4*, 2979−2993.

(15) Huang, S.; Wang, W.; Lee, S.; Kwo, J.; Chien, C. Intrinsic Spin-Dependent Thermal Transport. *Phys. Rev. Lett.* **2011**, *107*, 216604.

(16) Zhu, L.; Li, B.; Ma, H.; Qian, M.; Yao, K. Electrical-Field Tuned Thermoelectric Performance of Graphene Nanoribbon with Sawtooth Edges. *Nanotechnology* **2019**, *30*, 445204.

(17) Ding, G.; Hu, Y.; Li, D.; Wang, X.; Qin, D. Spin Seebeck Effect in Bipolar Magnetic Semiconductor: A Case of Magnetic Mos2 Nanotube. *J. Adv. Res.* **2020**, *24*, 391−396.

(18) Ni, Y.; Yao, K.; Fu, H.; Gao, G.; Zhu, S.; Wang, S. Spin Seebeck Effect and Thermal Colossal Magnetoresistance in Graphene Nanoribbon Heterojunction. *Sci. Rep.* **2013**, *3*, 1−5.

(19) Liu, Q.-B.; Wu, D.-D.; Fu, H.-H. Edge-Defect Induced Spin-Dependent Seebeck Effect and Spin Figure of Merit in Graphene Nanoribbons. *Phys. Chem. Chem. Phys.* **2017**, *19*, 27132−27139.

(20) Kan, E.-j.; Li, Z.; Yang, J.; Hou, J. Half-Metallicity in Edge-Modified Zigzag Graphene Nanoribbons. *J. Am. Chem. Soc.* **2008**, *130*, 4224−4225.

(21) Kim, W. Y.; Kim, K. S. Prediction of Very Large Values of Magnetoresistance in a Graphene Nanoribbon Device. *Nat. Nanotechnol.* **2008**, *3*, 408−412.

(22) Wang, W.; Li, Q.; Lv, D.; Liu, R.-j.; Peng, Z.; Yang, S. Monte Carlo Study of Magnetization Plateaus in a Zigzag Graphene Nanoribbon Structure. *Carbon* **2017**, *120*, 313−325.

(23) Zhu, S.-C.; Hu, T.-Y.; Wu, K.-M.; Lam, C.-H.; Yao, K.-L.; Sun, H.-R.; Yip, C.-T. Negative Differential Resistance Effect of Blue Phosphorene-Graphene Heterostructure Device. *J. Phys. Commun.* **2020**, *4*, No. 035005.

(24) Ozaki, T.; Nishio, K.; Weng, H.; Kino, H. Dual Spin Filter Effect in a Zigzag Graphene Nanoribbon. *Phys. Rev. B* **2010**, *81*, No. 075422.

(25) Xu, B.; Yin, J.; Xia, Y.; Wan, X.; Jiang, K.; Liu, Z. Electronic and Magnetic Properties of Zigzag Graphene Nanoribbon with One Edge Saturated. *Appl. Phys. Lett.* **2010**, *96*, 163102.

(26) Zeng, M.; Feng, Y.; Liang, G. Thermally Induced Currents in Graphene-Based Heterostructure. *Appl. Phys. Lett.* **2011**, *99*, 123114.

(27) Trabelsi, A. B. G.; Kusmartsev, F.; Robinson, B.; Ouerghi, A.; Kusmartseva, O.; Kolosov, O.; Mazzocco, R.; Gaifullin, M. B.; Oueslati, M. Charged Nano-Domes and Bubbles in Epitaxial Graphene. *Nanotechnology* **2014**, *25*, 165704.

(28) Zamborlini, G.; Imam, M.; Patera, L. L.; Mentes, T. O.; Stojic, N.; Africh, C.; Sala, A.; Binggeli, N.; Comelli, G.; Locatelli, A. Nanobubbles at Gpa Pressure under Graphene. *Nano Lett.* **2015**, *15*, 6162−6169.

(29) Levy, N.; Burke, S.; Meaker, K.; Panlasigui, M.; Zettl, A.; Guinea, F.; Neto, A. C.; Crommie, M. F. Strain-Induced Pseudo−Magnetic Fields Greater Than 300 Tesla in Graphene Nanobubbles. *Science* **2010**, *329*, 544−547.

(30) Guinea, F.; Geim, A.; Katsnelson, M.; Novoselov, K. Generating Quantizing Pseudomagnetic Fields by Bending Graphene Ribbons. *Phys. Rev. B* **2010**, *81*, No. 035408.

(31) Stolyarova, E.; Stolyarov, D.; Bolotin, K.; Ryu, S.; Liu, L.; Rim, K.; Klima, M.; Hybertsen, M.; Pogorelsky, I.; Pavlishin, I.; Kusche, K.; Hone, J.; Kim, P.; Stormer, H. L.; Yakimenko, V.; Flynn, G.

Observation of Graphene Bubbles and Effective Mass Transport under Graphene Films. *Nano Lett.* **2009**, *9*, 332−337.
(32) Dean, C. R.; Young, A. F.; Meric, I.; Lee, C.; Wang, L.; Sorgenfrei, S.; Watanabe, K.; Taniguchi, T.; Kim, P.; Shepard, K. L.; Hone, J. Boron Nitride Substrates for High-Quality Graphene Electronics. *Nat. Nanotechnol.* **2010**, *5*, 722−726.
(33) Son, Y.-W.; Cohen, M. L.; Louie, S. G. Energy Gaps in Graphene Nanoribbons. *Phys. Rev. Lett.* **2006**, *97*, 216803.
(34) Hübner, J.; Rühle, W.; Klude, M.; Hommel, D.; Bhat, R.; Sipe, J.; Van Driel, H. Direct Observation of Optically Injected Spin-Polarized Currents in Semiconductors. *Phys. Rev. Lett.* **2003**, *90*, 216601.
(35) Gong, K.; Zhang, L.; Ji, W.; Guo, H. Electrical Contacts to Monolayer Black Phosphorus: A First-Principles Investigation. *Phys. Rev. B* **2014**, *90*, 125441.
(36) Perdew, J. P.; Chevary, J. A.; Vosko, S. H.; Jackson, K. A.; Pederson, M. R.; Singh, D. J.; Fiolhais, C. Atoms, Molecules, Solids, and Surfaces: Applications of the Generalized Gradient Approximation for Exchange and Correlation. *Phys. Rev. B* **1992**, *46*, 6671.
(37) Perdew, J. P.; Wang, Y. Accurate and Simple Analytic Representation of the Electron-Gas Correlation Energy. *Phys. Rev. B* **1992**, *45*, 13244.
(38) Imry, Y.; Landauer, R. Conductance Viewed as Transmission. *Rev. Mod. Phys.* **1999**, *71*, S306.

https://doi.org/10.1021/acsomega.1c01640
ACS Omega 2021, 6, 15308−15315